

Design of a flat field concave-grating-based micro-Raman spectrometer for environmental applications

Zhiyun Li,¹ M. Jamal Deen,^{1,2,*} Qiyin Fang,^{1,3} and P. R. Selvaganapathy^{1,4}

¹School of Biomedical Engineering, McMaster University, 1280 Main Street West, Hamilton, Ontario L8S 4K1, Canada

²Department of Electrical and Computer Engineering, McMaster University, 1280 Main Street West, Hamilton, ON L8S 4K1, Canada

³Department of Engineering Physics, McMaster University, 1280 Main Street West, Hamilton, Ontario L8S 4K1, Canada

⁴Department of Mechanical Engineering, McMaster University, 1280 Main Street West, Hamilton, Ontario L8S 4K1, Canada

*Corresponding author: jamal@mcmaster.ca

Received 11 June 2012; revised 12 August 2012; accepted 15 August 2012;
posted 27 August 2012 (Doc. ID 170343); published 28 September 2012

In order to simplify the design process of microfabricated concave gratings, simplified algorithms for fast characterization of the concave grating were developed. These algorithms can be used to assist system designers using ray-tracing software in the determination of optimum design parameters considering the requirements and restrictions for specific applications. According to the algorithms, it is feasible to design a flat field microconcave grating with a 4 mm grating radius as a key component in a micro-Raman spectrometer system for inline environmental monitoring applications. This microspectrometer operates over the spectral wavelength band from 785 nm to 1000 nm and has a spectral resolution of 2 nm at 900 nm. The total size of the system is 1 mm × 4 mm × 3.7 mm, making it one of the smallest for this wavelength range and spectrum resolution. © 2012 Optical Society of America

OCIS codes: 050.1950, 050.2770, 080.2740, 080.1005, 120.6200, 170.5660.

1. Introduction

Water safety is a major concern in many countries throughout the world. Harmful chemicals and bacteria in the water supply pose significant health risks for humans. To monitor water quality and improve water safety, a low-cost, compact, sensitive, and easy-to-use detection system is required. For monitoring chemical and biological contaminants in water, optical methods have attracted much interest due to their noncontacting and nondestructive properties [1–3]. Among the various optical techniques being considered, Raman spectroscopy, as a chemical composition characterization technique, possesses several advantages over other optical methods in water

monitoring and other applications [4]. For example, there is flexibility in the choice of excitation source, which can suppress the strong absorption by water in the infrared region.

A typical Raman spectrometer usually involves a planar dispersive element, a collimating mirror, and a focusing mirror. However, these spectrometers are mainly limited to laboratory use because of their complex arrangement, large size, and high cost. Recently, planar-grating-based microspectrometers [5,6] have been proposed with good performance in spectral resolution. However, the use of planar gratings still restricts their miniaturization, especially when it comes to the microsized spectrometers.

On the other hand, a concave grating has great potential for the miniaturization of a Raman spectrometer. This is because of its ability to achieve both wavelength separation and light focusing without

additional auxiliary optical components [7]. In 2008, a concave-grating-based microspectrometer of total size of 11 mm × 5 mm × 6 mm was reported [8]. However, the design was aimed at a broad wavelength band (400–1030 nm) and the spectrum resolution in near infrared region was about 5 nm. In [9], a microspectrometer with 44.4 mm grating radius that achieved 0.9 nm resolution at 1550 nm was reported. However, the circular horizontal focal curve of the grating makes it difficult to be focused onto a flat field image sensor.

The design of a concave grating usually involves the analysis of optical path function and optimization of aberrations for different grating configurations (Rowland or flat field) [10,11], a very cumbersome process. Therefore, to simplify the design process and achieve fast characterization of the system's performance, a simplified algorithm based on aberration theory was developed. Based on this algorithm, the system's spectral resolution can be calculated for different system parameters. This is very helpful in determining the optimum combination of the design parameters for specific applications and benefits the optical design using ray tracing software. This algorithm was also used to design a flat field concave-grating-based micro-Raman spectrometer that covers the near infrared region with sufficient spectral resolution for Raman spectroscopy [12,13].

2. Theory

The schematic diagram of a Rowland-configuration-based concave grating is illustrated in Fig. 1. The larger circle, Grating circle (blue) with radius R and center O , represents the grating and the smaller one (red) with diameter R is the Rowland circle [7]. In a Rowland configuration, the entrance slit is placed on the Rowland circle. Points X and Y are two arbitrary points on the grating curvature and OX and OY are their normal, respectively. If the arc length XY is small compared to the grating radius R , then X and Y can be assumed to also be on the Rowland circle. In this case, the incident angles α and γ are identical.

According to the grating Eq. (1) for a certain diffraction order m , wavelength λ , and groove density G , the same incident angles have the same

diffraction angles, which means that β and δ in Fig. 1 are also identical.

$$\sin \alpha + \sin \beta = mG\lambda. \quad (1)$$

Therefore, light of wavelength λ diffracted from different points of the grating will intersect with the Rowland circle at the same point [$B1$ ($\lambda1$) or $B2$ ($\lambda2$)], which gives rise to the focusing property of a concave grating.

3. Grating Design

In designing a concave-grating-based spectrometer system, there are several important parameters, including the wavelength band, grating period, grating radius, and incident angle. Since we are interested in monitoring for bacteria and chemical contaminants in drinking water, then we need to suppress the influence of fluorescence and guarantee adequate quantum efficiency of silicon image sensor. Therefore, the excitation source is chosen to be a 785 nm laser. Based on this excitation source and considering the absorption limitation of silicon-based detectors at longer wavelengths above 1000 nm, the wavelength band of this design was set to be between 785 nm and 1000 nm, which is adequate for our application. This choice is because the Raman shift for most bacterial and chemical contaminants is between 500 cm^{-1} and 2000 cm^{-1} [1,14], and the Raman signal is between 817 nm and 931 nm consequently, which is inside the wavelength band we have set. With this wavelength band, the grating period and incident angle can be determined through simulations of the diffraction efficiency.

A grating simulation program, Pegrade (I.I.G., Inc., New York, USA) [15], was used in this work. According to the simulation results, the incident angle is set to be between 20° and 40°. In Fig. 2, the simulation results of diffraction efficiency with different grating periods, assuming a 30° incident angle and an Al-coated sinusoidal grating, are presented. Based on the results in Fig. 2, the grating period used in this work was set to be 1 μm .

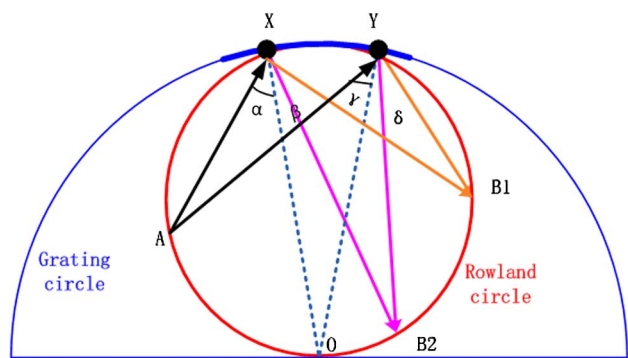


Fig. 1. (Color online) Rowland-configuration-based concave grating.

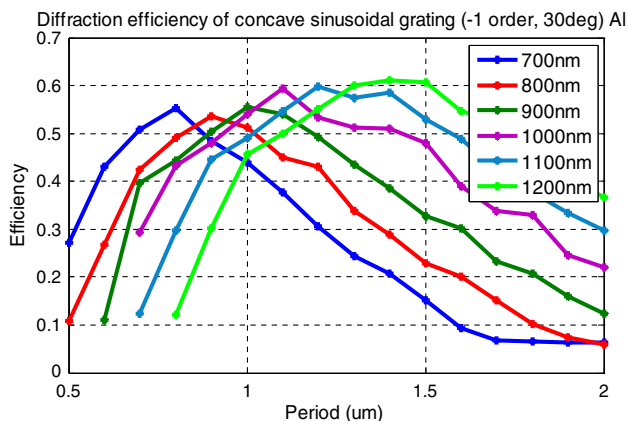


Fig. 2. (Color online) Diffraction efficiency with different grating periods.

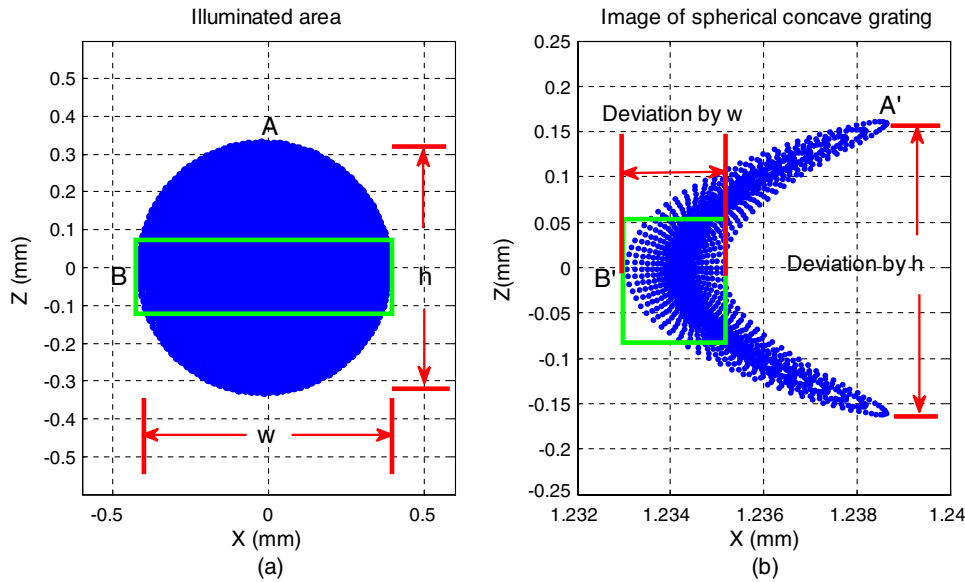


Fig. 4. (Color online) (a) Illuminated area of a point source. (b) Image of a point source.

First, a point source usually illuminates a grating with an area of height h and width w [see Fig. 4(a)]. Generally, the height h is close to the width w or in the same order of magnitude. From the simulation results in Fig. 4, light diffracted from A and B intersect with the image plane at A' and B' , respectively. In this case, the largest horizontal deviation, which determines $\Delta\lambda_{\text{aberration}}$, will be caused by A rather than B . If z_p is the vertical coordinate of A , then the horizontal coordinate x_p will be very small. Therefore, Eq. (6) can be simplified as Eq. (8) and is

$$D_h = \frac{r_b}{\cos \beta} \frac{\partial F}{\partial x_p} = \frac{r_b}{\cos \beta} \left(\frac{1}{2} z_p^2 F_{12} + \frac{1}{24} z_p^4 F_{14} + \dots \right), \quad (8)$$

with $F_{12} = \frac{\sin \alpha}{r_{\text{in}}} \left(\frac{1}{r_{\text{in}}} - \frac{\cos \alpha}{R} \right) + \frac{\sin \beta}{r_b} \left(\frac{1}{r_b} - \frac{\cos \beta}{R} \right)$ and

$$F_{14} = \frac{3 \sin \alpha}{R^2 r_{\text{in}}^2} (1 - 3 \cos^2 \alpha) - \frac{9 \sin \alpha}{r_{\text{in}}^4} + \frac{3 \sin \alpha \cos \alpha}{R r_{\text{in}}} \left(\frac{6}{r_{\text{in}}^2} - \frac{1}{R^2} \right) + \dots + \frac{3 \sin \beta}{R^2 r_b^2} (1 - 3 \cos^2 \beta) - \frac{9 \sin \beta}{r_b^4} + \frac{3 \sin \beta \cos \beta}{R r_b} \left(\frac{6}{r_b^2} - \frac{1}{R^2} \right).$$

With the increase of $(i+j)$, the contribution of higher-order aberration to the total resolution becomes smaller and only $(i+j) \leq 5$ terms are considered in this work. Therefore, with F_{12} and F_{14} , the aberration contribution can be calculated using

$$\Delta\lambda_{\text{abr}} = \frac{d}{m} \left(\frac{1}{2} z_p^2 F_{12} + \frac{1}{24} z_p^4 F_{14} \right). \quad (9)$$

Using Eqs. (8) and (9), Fig. 5(a) gives the variation of F_{12} and F_{14} as a function of incident angle.

Figure 5(b) shows the aberration contribution when considering F_{12} and $(F_{12} + F_{14})$, respectively. From the calculations shown, we concluded that considering only F_{12} is adequate to quantify the aberration contribution. Although $|F_{12}|$ is smaller than $|F_{14}|$, considering the fact that z_p is also very small, this causes the first term on right side of Eq. (9) to be much larger than the second term. For the purposes of further simplifying the calculation process, F_{12} is simplified, and Eq. (9) can now be rewritten as

$$\Delta\lambda_{\text{abr}} = \frac{1}{2} \frac{d}{m} z_p^2 \left(\frac{\sin \alpha}{r_{\text{in}}} \left(\frac{1}{r_{\text{in}}} - \frac{\cos \alpha}{R} \right) + \frac{mG\lambda - \sin \alpha}{r_b^2} - \frac{mG\lambda - \sin \alpha}{R r_b} + \frac{(mG\lambda - \sin \alpha)^3}{2R r_b} \right). \quad (10)$$

However, in some situations, mirrors are used to restrict light transmission in some direction, functioning like a waveguide. In this case, the spot height h will be much smaller than spot width w (green area in Fig. 4). Therefore, the largest horizontal deviation will be caused by point B , rather than point A . If (x_p, y_p, z_p) is the coordinate of point B , z_p will be close to zero. In this case, the aberration relevant contribution can be calculated by using Eq. (11) (Rowland configuration, $F_{20} = F_{30} = 0$), and is

$$\Delta\lambda_{\text{abr}} = \frac{d}{m \cos \beta} \frac{r_b}{\partial x_p} = \frac{d}{m \cos \beta} \left(\frac{1}{6} x_p^3 F_{40} + \frac{1}{24} x_p^4 F_{50} + \frac{1}{120} x_p^5 F_{60} + \dots \right). \quad (11)$$

Based on Eq. (11), Fig. 6 shows the variation of resolution with incident angle when considering only F_{40} , $(F_{40} + F_{50})$ and $(F_{40} + F_{50} + F_{60})$. According to the

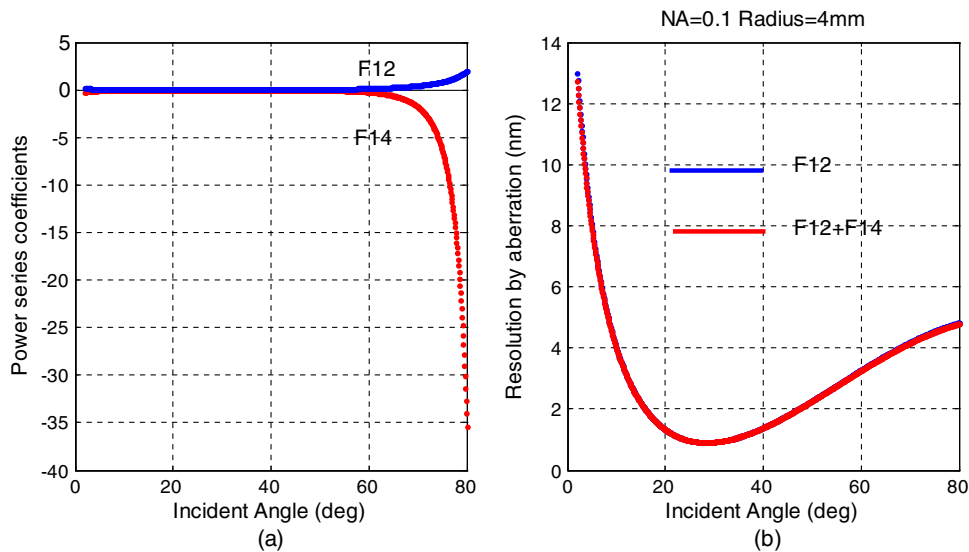


Fig. 5. (Color online) (a) Power series coefficients with different incident angle. (b) Resolution when considering different power series coefficients.

calculation, the deviation mainly happens when using a large incident angle ($>60^\circ$) or a very small incident angle ($>10^\circ$). Since the incident angle of this work is between 20° and 40° , using only the F_{40} term is enough to calculate the aberration contribution.

Note that F_{40} is given by

$$F_{40} = \frac{3 \cos^2 \alpha}{r_{in}^3} (5 \sin^2 \alpha - 1) + \frac{6 \cos \alpha}{R r_{in}^2} (1 - 3 \sin^2 \alpha) + \frac{3 \sin^2 \alpha}{R^2 r_{in}} - \frac{3 \cos \alpha}{R^3} \dots + \frac{3 \cos^2 \beta}{r_b^3} (5 \sin^2 \beta - 1) + \frac{6 \cos \beta}{R r_b^2} (1 - 3 \sin^2 \beta) + \frac{3 \sin^2 \beta}{R^2 r_b} - \frac{3 \cos \beta}{R^3}. \quad (12)$$

For the Rowland configuration, F_{40} can be further simplified as

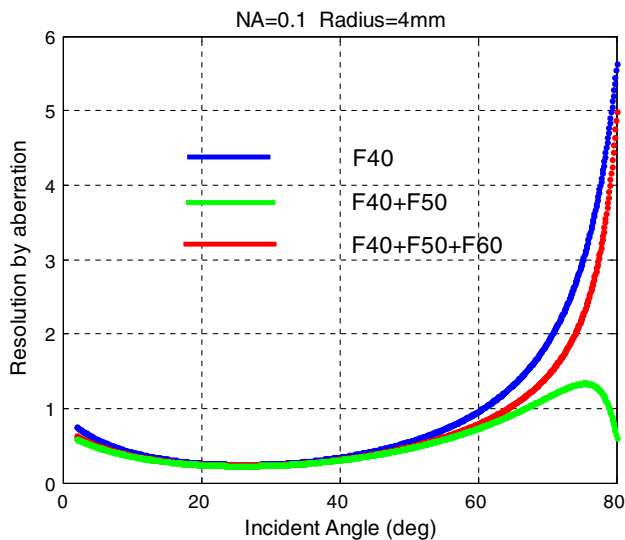


Fig. 6. (Color online) Resolution caused by spot width when considering different number of power series coefficients.

$$F_{40} = \frac{3}{R^3} \left(\frac{1}{\cos \alpha} - \cos \alpha \right) + \frac{3(mG\lambda - \sin \alpha)^2}{R^3 \left(1 - \frac{1}{2}(mG\lambda - \sin \alpha) \right)}. \quad (13)$$

Equation (13) has been tested using the parameters in [9]. The result of the calculations is ~ 1 nm resolution, which is in very good agreement with both the calculations (0.9 nm) and measurements (1.1 nm) reported in [9]. Equation (10) is tested by applying to the data in [18], which gives a spectrum resolution of $\Delta\lambda = \sqrt{\Delta\lambda_{abr}^2 + \Delta\lambda_{En}^2 + \Delta\lambda_{diff}^2} = \sqrt{0.94^2 + 0.19^2 + 0.15^2} = 0.97$ nm. This result is close to the measured spectral resolution of 0.9 nm in [18]. Figure 7(a) shows the ray tracing result of a concave grating by Zemax. Figure 7(b) shows the spot diagram of a point source under four different incident angles from 20° to 70° . The colors in Fig. 7(b) represent three different wavelengths with 1.5 nm step. According to the ray tracing results in Fig. 7, a 35° incident angle gives better resolution than other angles, and the spectral resolution of a point source under 35° incident is about 1.5 nm, which proves the calculation result by aberration theory in Fig. 5(b) of $\sqrt{\Delta\lambda_{abr}^2 + \Delta\lambda_{diff}^2} = \sqrt{1.09^2 + 1.13^2} = 1.57$ nm.

After combining all the contributions from aberration, diffraction limitation, and entrance slit, the overall resolution is obtained. Figure 8 gives the dependence of the total resolution on different system's parameters of both situations discussed above: when the height h is close to the width w [Fig. 8(a)], or when h is much smaller than w [Fig. 8(b)].

The numerical aperture (NA) in Fig. 8 refers to the NA of the entrance fiber. Based on the results in Fig. 8, the value of total resolution decreases with decreasing NA at first (stage 1), then it reaches the minimum value at about 0.1, after which, the

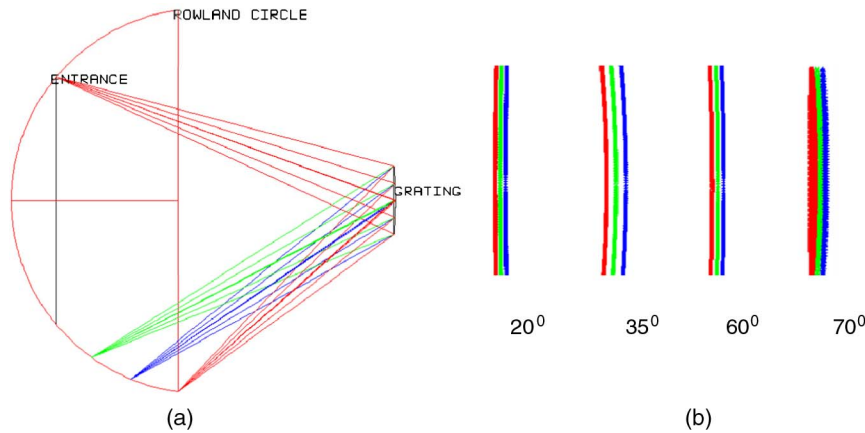


Fig. 7. (Color online) (a) Ray tracing of a point source by Zemax. (b) Spot diagram of three different wavelengths, including 900 nm, 901.5 nm, and 903 nm.

resolution changes in the opposite way, with a further decreased NA (stage 2). Among the three contributions, $\Delta\lambda_{\text{Entrance}}$ is independent of NA, $\Delta\lambda_{\text{Aberration}}$ is proportional to NA, and $\Delta\lambda_{\text{Diffraction}}$ is inversely proportional to NA. For stage 1, $\Delta\lambda_{\text{Aberration}}$ changes faster than $\Delta\lambda_{\text{Diffraction}}$; therefore, total resolution is proportional to the NA. After the minimum point is reached, $\Delta\lambda_{\text{Diffraction}}$ changes faster than $\Delta\lambda_{\text{Aberration}}$, and the overall trend is inversely proportional to NA in stage 2. Moreover, a large grating radius has a better resolution due to the relatively smaller aberration. Therefore, to achieve good resolution, most concave gratings use large grating radii. Based on the requirements and limitations of the specific applications, the above

algorithms can be used to determine the optimum combination of different design parameters. Since our target is a microspectrometer for inline monitoring, then the grating radius was chosen to be 4 mm. With this radius, according to the results in Fig. 8, reasonable resolutions were obtained.

4. Flat Field Concave Grating

One important disadvantage of concave grating is the circular horizontal focal curve. Setting $F_{20} = 0$, then r_b in F_{20} , together with the diffraction angle β from grating equation, give the horizontal focal curve. Since the image sensor typically has a planar photosensitive area [19], then using such a planar surface to collect diffraction light from concave

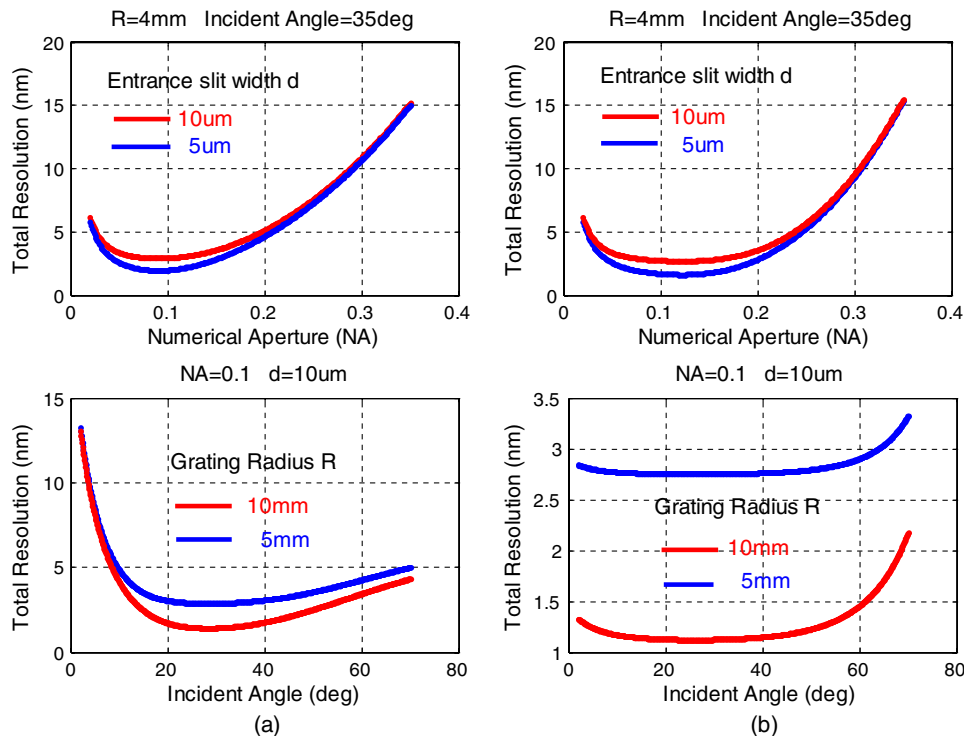


Fig. 8. (Color online) Total resolutions when (a) the height h is close to the width w , and (b) the height h is much smaller than the width w .

gratings will make the resolution worse. Considering the fact that a concave surface imager sensor is not common, then a flat field concave grating (linear focal curve) is a better solution to this problem. For a concave grating with constant groove density in the x direction, F_{20} is given by

$$F_{20} = \left(\frac{\cos^2 \alpha}{r_{in}} - \frac{\cos \alpha}{R} \right) + \left(\frac{\cos^2 \beta}{r_b} - \frac{\cos \beta}{R} \right). \quad (14)$$

To change the shape of the horizontal focal curve, one effective way is to use the varied line space concave grating, by which, $\frac{\partial^i(mN\lambda)}{\partial x^i} \neq 0$ and the power series coefficients can be rewritten [11] as

$$F_{ij} = M_{ij} + mG_0\lambda H_{ij}. \quad (15)$$

In Eq. (15), the first term M_{ij} on right side is determined by the mounting information of the grating, such as the positions for entrance slit, grating, and image plane. Note that H_{ij} is relevant to the groove density distribution along the x direction and it can be determined based on the optimization of the focal curve and aberration. Also, G_0 is the groove density at the grating center. To determine the structural information, each of the H_{ij} terms should be solved. Therefore, in this work, specific algorithms are derived for calculating the parameters of the flat-field concave grating.

A reference point Q_0 is picked from the horizontal focal curve at first, and the wavelength corresponding to Q_0 is λ_0 . To make the focal curve linear, the slope k_{QQ_0} between the reference point $Q_0(\lambda_0 \ x_0 \ y_0)$ and any other point $Q(\lambda \ x \ y)$ should be constant. That is,

$$k_{QQ_0} = \frac{y - y_0}{x - x_0} = C, \quad (16)$$

where $x_0 = r_{b0} \sin \beta_0$, $y_0 = R - r_{b0} \cos \beta_0$, $x = r_b \sin \beta$, $y = R - r_b \cos \beta$.

Applying the grating equation to Eq. (16), the slope between Q and Q_0 can be written as

$$k_{QQ_0}(t) = \frac{r_{b0} \cos \beta_0 - r_b \cos \beta}{r_b \sin \beta - r_{b0} \sin \beta_0} = \frac{r_{b0} \sqrt{1 - (mG_0\lambda_0 - \sin \alpha)^2} - r_b \sqrt{1 - t^2}}{r_b \cdot t - r_{b0}(mG_0\lambda_0 - \sin \alpha)}, \quad (17)$$

where $r_b = \frac{\cos^2 \beta}{\frac{\cos \beta}{R} - mG_0\lambda H_{20}} = \frac{R(1-t^2)}{(1-t^2)^{\frac{1}{2}} - R \cdot t H_{20} - R \sin \alpha H_{20}}$, $t = mG_0\lambda - \sin \alpha$.

For a power series expansion of Eq. (17) in terms of t , we get

$$k_{QQ_0}(t) = g(t) = g_0 + g'(0)t + \frac{1}{2}g''(0)t^2 + \frac{1}{6}g'''(0)t^3 + \dots \quad (18)$$

To guarantee a constant slope, which means keeping only the g_0 term, then the sum of all other terms is set to zero. The idea of a flat field concave grating is to find a specific H_{20} which makes the sum of all “ t ” terms in Eq. (18) close to zero. To avoid the effect of “pole point” and to make the focal curve stable, the reference wavelength should be chosen out of the wavelength band. Using the Taylor’s expansion formula, the best H_{20} is found to be

$$H_{20} = \frac{\sqrt{mG_0\lambda_0 - \sin \alpha}}{RmG_0\lambda_0}. \quad (19)$$

Besides H_{20} , other H_{ij} terms can also be determined to reduce aberration such as coma and spherical aberration. After determining all of the H_{ij} terms, the groove density can be written as

$$G = G_0 \times \left(1 + H_{20}x + \frac{1}{2}H_{30}x^2 + \frac{1}{6}H_{40}x^3 \right). \quad (20)$$

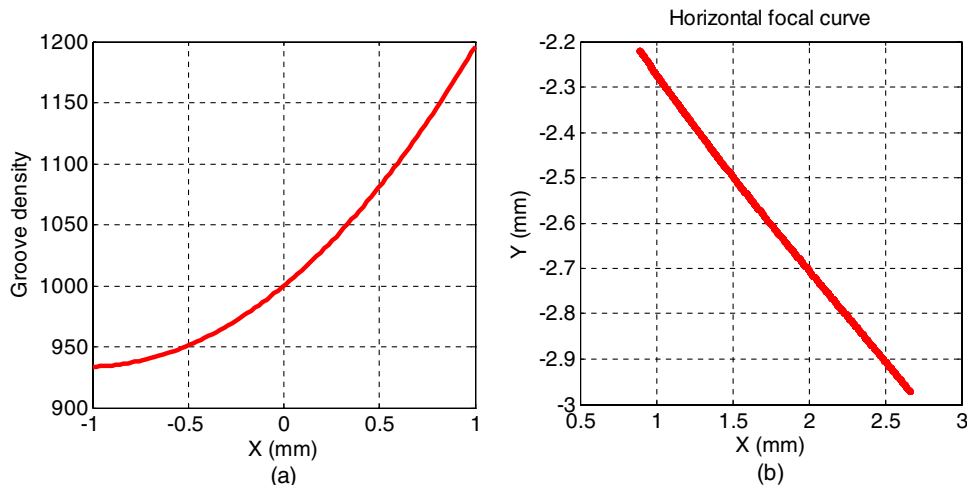


Fig. 9. (Color online) (a) Groove density variation in x direction. (b) Horizontal focal curve.

Table 1. Parameters for Two Types of Different Configurations at 900 nm

	F_{20}	F_{02}	F_{30}	F_{12}	F_{40}	F_{04}	F_{22}	$\Delta\lambda_{abr}$ (nm)	$\Delta\lambda_{diff}$ (nm)	$\Delta\lambda_{en}$ (nm)	$\Delta\lambda_{Tot}$ (nm)
A	0	0.13	0	0.02	0.024	0.09	0.02	1.09	1.13	1.25	2.00
B	0	-0.002	0	0.013	-9.6E-05	0.05	0.01	0.71	1.13	1.25	1.83
C	0	0.026	0	0.025	4.4E-03	0.06	0.02	1.17	1.13	1.25	2.04

A—Constant space, 35° incident, 1 μm groove density;

B—Varied space, 35° incident;

C—Varied space, 40° incident.

Since the wavelength band of our application was between 785 nm and 1000 nm, then the reference wavelength was chosen to be 1400 nm, which gave a value for H_{20} of ~ 0.13 . Then, H_{30} and H_{40} are calculated to be 1.38×10^{-2} and 7.3×10^{-3} , respectively. Other parameters that were used include the center grating period (1 μm), radius (4 mm), and incident angle (40°). Figure 9(a) gives the groove density along the x direction and Fig. 9(b) shows the horizontal focal curve of the varied space concave grating.

As we can see from Fig. 9(b), the focal curve has been changed to be linear and the distance from the grating to image plane is also increased. Due to the increased distance and reduced aberration, the aberration contribution to resolution in this case is better than constant space concave grating. Table 1 gives the detailed information for both a constant line space concave grating and a varied line space, flat field concave grating. The parameters used for the entrance slit include the NA (0.1) and diameter (5 μm). Based on the results in Table 1, both the

constant space and varied line space concave gratings provide a resolution better than 2 nm. To avoid the interference between the incident beam and the diffraction beam, the incident angle of the varied space grating is set to 40°.

According to the parameters in Table 1, Fig. 10 shows the schematic diagram of the concave micrograting system. In this system, a baffle was added to avoid direct illumination from the entrance to the detector. To make the whole system more compact, a mirror was used to reflect the diffraction beams to detector1, and the total size is about 1 mm × 4 mm × 3.7 mm. This compact system covers a wavelength band from 785 nm to 1000 nm, while the area we are interested is between 817 nm and 931 nm as mentioned above. This wavelength range is marked by the green dashed lines in both detector and detector1.

5. Conclusions

A concave micrograting with 4 mm grating radius is designed and modeled. To simplify the design process and achieve rapid calculation for spectral resolution, simplified algorithms have been developed based on the aberration theory. To further solve the problem associated with the circular horizontal focal curve, the design of a varied line space concave grating is discussed and relevant algorithms are derived. Using the theory and algorithms developed, an example design of a microspectrometer using this concave micrograting of total size 1 × 4 × 3.7 mm³ is demonstrated. This grating is one of the smallest ones for wavelength band of 785 to 1000 nm, and it demonstrated excellent spectral resolution of ~ 2 nm at 900 nm and ~ 2.3 nm at 1000 nm. Although the system NA (0.1) is sacrificed for a compact system, this compromise will be ameliorated by employing a high-sensitivity photon detection system such as one based on single photon avalanche photodiodes. Finally, because of its compact size and spectral characteristics, the proposed concave micrograting can be used in optical systems for monitoring bacteria and chemical contaminants in drinking water.

The authors gratefully acknowledge Natural Sciences and Engineering Research Council of Canada (NSERC), Ontario Ministry of Research & Innovation (ERA program), and the CRC program for financially supporting the research work. MJD acknowledges the ITCE Division, POSTECH, under the sponsorship of WCU-MEST-NRF of Korea (R31-10100), where

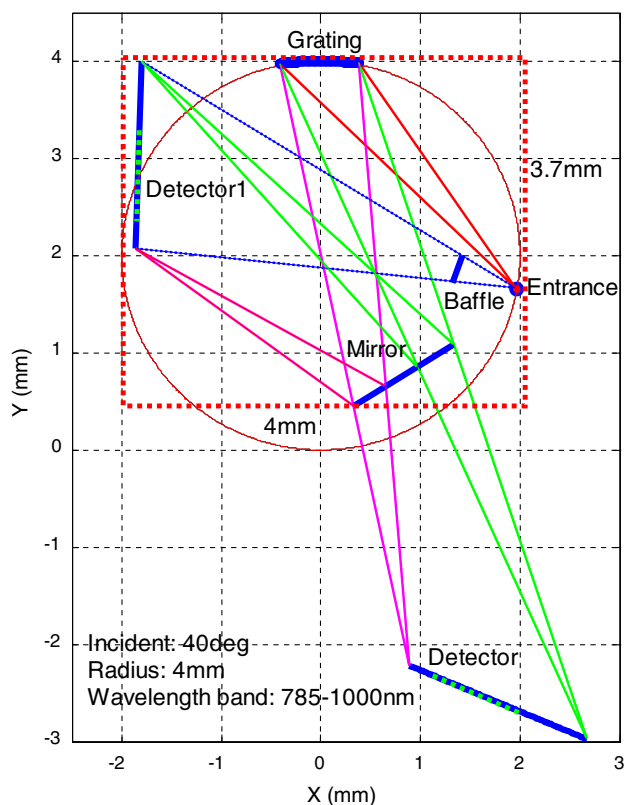


Fig. 10. (Color online) Schematic diagram of concave micrograting spectrometer system.

he was a Distinguished Visiting Professor during the final preparation of this paper.

References

1. Q. Wu, T. Hamilton, W. H. Nelson, S. Elliott, J. F. Sperry, and M. Wu, "UV Raman spectral intensities of *E. coli* and other bacteria excited at 228.9, 244.0, and 248.2 nm," *Anal. Chem.* **73**, 3432–3440 (2001).
2. M. M. Mariani, P. J. Day, and V. Deckert, "Applications of modern micro-Raman spectroscopy for cell analyses," *Integr. Biol.* **2**, 94–101 (2010).
3. T. Ilescu, M. Baia, and V. Miclaus, "A Raman spectroscopic study of the diclofenac sodium-beta-cyclodextrin interaction," *Eur. J. Pharmaceut. Sci.* **22**, 487–495 (2004).
4. M. J. Deen and E. D. Thompson, "Design and simulated performance of a CARS spectrometer for dynamic temperature measurements using electronic heterodyning," *Appl. Opt.* **28**, 1409–1416 (1989).
5. R. F. Wolffenbuttel, "State-of-the-art in integrated optical microspectrometers," *IEEE Trans. Instrum. Meas.* **53**, 197–202 (2004).
6. S. Grabarnik, A. Emadi, E. Sokolova, G. Vdovin, and R. F. Wolffenbuttel, "Optimal implementation of a microspectrometer based on a single flat diffraction grating," *Appl. Opt.* **47**, 2082–2090 (2008).
7. T. Namilka, "Theory of the concave grating," *J. Opt. Soc. Am.* **49**, 446–460 (1959).
8. R. Brunner, M. Burkhardt, K. Rudolf, and N. Correns, "Microspectrometer based on holographically recorded diffractive elements using supplementary holograms," *Opt. Express* **16**, 12239–12250 (2008).
9. H. K. Cheng, "Micrograting fabricated by deep x-ray lithography for optical communications," *Opt. Eng.* **46**, 048001 (2007).
10. R. Grange, "Aberration-reduced holographic spherical gratings for Rowland circle spectrographs," *Appl. Opt.* **31**, 3744–3749 (1992).
11. C. Palmer and E. G. Loewen, *Diffraction Grating Handbook* (Newport Corporation, 2005).
12. W. R. Premasiri, D. T. Moir, M. S. Klemperer, N. Krieger, G. Jones II, and L. D. Ziegler, "Characterization of the surface enhanced Raman scattering (SERS) of bacteria," *J. Phys. Chem. B* **109**, 312–320 (2005).
13. C. Xie and Y. Li, "Confocal micro-Raman spectroscopy of single biological cells using optical trapping and shifted excitation difference techniques," *J. Appl. Phys.* **93**, 2982–2986 (2003).
14. R. K. Dutta, P. K. Sharma, and A. C. Pandey, "Surface enhanced Raman spectra of *Escherichia coli* cell using ZnO nanoparticles," *Dig. J. Nanomater. Biostruct.* **4**, 83–87 (2009).
15. "PCGrates," <http://www.iigrate.com/about/pcgrates>.
16. A. C. Thompson and D. Vaudh, *X-Ray Data Booklet*, 2nd ed. (Lawrence Berkeley Laboratory, 2001).
17. E. G. Loewen, *Diffraction Gratings and Applications* (Marcel Dekker, 1997).
18. S. Grabarnik, "Concave diffraction gratings fabricated with planar lithography," *Proc. SPIE* **6992**, 1–8 (2008).
19. M. J. Deen and P. K. Basu, *Silicon Photonics—Fundamentals and Devices* (Wiley, 2012).